Graphene Oxide Fibers: Synthesis Method and Correlation among Compositional, Vibrational, and Electrical Properties

J. R. Castro-Ladino
Universidad de los Llanos https://orcid.org/0000-0003-2961-2732
J. J. Prías-Barragán (jjprias@uniquindio.edu.co)
Universidad del Quindío https://orcid.org/0000-0001-9058-2187

Research Article

Keywords: Graphite oxide fibers, rice husk, vibrational properties, electrical properties

Posted Date: September 27th, 2022

DOI: https://doi.org/10.21203/rs.3.rs-2086987/v1

Abstract

The synthesis method and correlation among compositional, vibrational, and electrical properties in graphene oxide fibers (GOF) are presented and discussed here. The GOF samples were synthesized from rice husk (RH) as source material, via a thermal decomposition method employing an automated pyrolysis system with a controlled nitrogen atmosphere, varying carbonization temperature (T_{CA}) from 773 to 1273 K. The samples were characterized through scanning electron microscopy (SEM), X-ray photoelectron spectroscopy (XPS), Raman spectroscopy, and current-voltage curves at four points of collinear electrical contacts. Oxide concentration (OC) of samples varied from 0.21 (at T_{CA} = 1273 K) to 0.28 (T_{CA} = 773 K), influenced by T_{CA}. The GOF samples exhibited fiber morphology composed of porous structures with sizes between 5 and 30 *μm*; peaks in the XPS spectrum at ≈ 538 and 284 *eV* were associated with O1s and C1s, respectively. Analysis of the results corroborates the graphite oxide vibrational behavior with crystal sizes varying from 3.52 to 4.88 *nm*, and boundary defects density of 3.12-3.6 x 10^{-4} cm^{-2}, as expected. The electrical response shows that OC decreases and increases electrical conductivity from 4.66 x 10^{-2} to 4.45 *S/m* at the polycrystalline phase, possibly attributed to the desorption of some oxides and organic compounds. Likewise, the physical correlations between OC and vibrational response revealed that decreased OC generates an increase in boundary defects density and decreased crystal size, as a consequence of thermal decomposition processes. The correlations between electrical and vibrational properties revealed that increased electrical conductivity increases defects density and decreases crystal size in GOF samples, possibly attributed to hydroxyl and epoxy bridges getting carbons atoms out of plane and modifying the band-gap energy (E_g) and graphitic structure. These results suggest that by controlling the T_{CA} and OC in the synthesis of GOF samples, modification of vibrational and electrical properties, of great interest in the electronic development of sensors and devices, has been made possible.

1. Introduction

Graphene materials that include black carbon, carbon nanotubes, and graphene, among others, have aroused great interest in basic and applied research[1–4]. However, these high-quality materials have a considerable cost and low availability. Precursor material from biomass, such as rice husk (RH) is an alternative low-cost, highly available, green method to produce carbon materials[5–9], like GOF. Rice husk is an abundant agro-industrial waste product, which can generate negative impacts on the environment, as well as on human and animal health; however, it has interesting compositional characteristics, as reported by Teo, E.Y.L., *et al.*[6], among others[10–12]. This aspect promotes RH as an alternative precursor in the production of graphite oxide materials[1,4,5]. Also, these materials are important in applications, such as green nanocomposites[10], supercapacitors[4,13–16], conductive materials[17], adsorbent materials[1,18], nanomaterials in biomedical applications[9,19,20], batteries[21,22], electronic devices[20,23], solar cells[24], and sensors[16,25,26], among others.

Numerous methods have been developed to synthesize GO, including Hummers' and its variants, Brodie's Staudenmaier's, and chemical vapor deposition (CVD,) among others[27,28]. However, these methods are complex and involve using toxic materials and solutions that harm the environment. Recently, biomass materials have been used to prepare materials based on graphene by employing the thermal decomposition method[27,29]. Also, first-stage thermal decomposition (FSTD) has been employed to synthesize GO from biomass precursors, like bamboo and RH[5,30].

Several works have synthesized GO and reduced graphene oxide (rGO) using traditional methods[28,31,32] and recently, it was synthetized via a FSTD method, employing RH biomass as source material[10,29,33,34]; furthermore, their morphological, compositional, vibrational, electrical, and physicochemical properties have been studied[5,10,35–39] and the effect of T_{CA} on these physical properties has been reported[23,40,41], in addition to their possible technological applications[5,42–44]. Moreover, some studies revealed that physical properties in GO can be influenced by tuning oxide concentrations[45–50]. Then, different experiments were carried out to measure the electrical response of GO via I-V curves method[50–52], showing that the temperature level of the medium in which the experiment is performed and the reduction or synthesis temperature influences electrical conductivity and the OC[45,46,50,53]. The vibrational characteristics were analyzed via Raman; the Raman spectrum of GO shows general features around 1360, 1600, and $2700 cm^{-1}$, which correlate with D, G, and 2D bands, respectively[5,10,33,46]. The OC variation generates significant changes in the GO Raman spectrum, such as the shift and intensity variation of the D and G bands, as a result of the modification of the functional groups, as well as the 2D and D + G bands and variation in the I_D/I_G ratio[45,48,54]. Additionally, in the FTIR spectra, it has been reported that changes in the position and intensities of the peaks in GO samples can be attributed to the different levels of OC[46,55]. Compositional characteristics have been studied employing XPS and two main peaks at 284 and $531 eV$ were observed and attributed to C1s and O1s, respectively; as the OC increases, the intensity of the C–C peak due to the sp^2 carbon bond in graphite gradually decreases, and increases the intensity of peaks associated to functional groups, such as hydroxyl, carboxyl, and epoxy groups[39,45,48].

However, although these physical properties have been studied in GO, the correlation among these physical properties in GOF is still unknown. Therefore, this work presents the correlation among the compositional, vibrational, and electrical properties, and the effect of the OC, crystal size, and defects density on the electrical conductivity of GOF samples. Also, the synthesis procedure is presented in GO samples obtained from the RH by using the FSTD method, the OC was estimated through XPS analysis, and the vibrational characteristics were measured via Raman spectroscopy.

2. Materials And Methods

The GOF samples were synthesized via the FSTD method in a controlled pyrolysis system. As a result of several tests and analyses, the protocol presented in Fig. 1a for synthesis of GOF samples from RH was established. Once the RH is deposited into the reactor, vacuum is generated for 3 min with the pump's action. Then, nitrogen flow is provided for 3 min with the vacuum pump activated, meaning, there is

nitrogen flow through the system and the pump exerts the suction action of the gases present, including the nitrogen. The vacuum pump is deactivated and the nitrogen is allowed to flow for another 3 min through the pyrolysis system. Execution of this protocol generates the inert atmosphere to avoid the thermal decomposition of the material and achieve its carbonization. The GOF samples were mechanically ground in a mortar to a particle size $< 180\mu m$, which was verified by passing the material through a Ro-Tap Model E sieve. In all the procedures and methods applied in the development of this work, the relevant standards were considered. The GOF samples were coded as S-T_{CA}, for example, code S-973 corresponds to a sample synthesized to 973 K. The authors confirm that all methods in experimental research and field studies on waste products of the commercial rice husk, were performed in accordance with the relevant regulations.

2.1. Characterization techniques

To obtain the SEM micrographs, the samples were fixed onto a graphite tape, a thin gold (Au) coating was applied (DENTON VACUUM Desk IV equipment) and they were analyzed in the JEOL JSM 6490 LV scanning electron microscope, using a high vacuum to obtain the images. The secondary electron detector was used to evaluate the morphology and topography of the samples.

The compositional analysis was performed through XPS, using a Spec photoelectron X-ray spectrometer (NAP-XPS) with a monochromatic Al Kα $hv = 1486.7eV$ source. Raman measurements were carried out at room temperature by employing a confocal Horiba Jobin Yvon, Model Labram HR, Raman spectrometer with an excitation HeNe laser beam working at a $632nm$ wavelength and $17mW$. All spectra were acquired under the same conditions in a range from 100 to 3500 cm^{-1}. The sheet resistance value was measured via electrical characterization at the four-point method with collinear electrical contacts. In this method, a constant current is applied to two of the tips, and the potential of the other two tips is measured with a high-impedance voltmeter. The GOF samples, as powders compacted at $1kg$ of force, were performed by injecting current in a range of -100 to $+100nA$ at four points, as a configuration of electrical contacts[23]. For the XPS, Raman, and electrical conductivity analyses, the GOF samples were mechanically ground in a mortar to particle size < 180 μm, verified by passing the material through a Ro-Tap Model E sieve.

3. Results And Discussion

3.1. Oxide concentrations

The oxide concentration (OC) was quantitatively determined by Eq. (1), deduced from the method presented by Carvalho *et al*., in[56], based on the peak-to-peak binding energy difference of the high-resolution XPS C1s spectrum.

$$OC = \left(\frac{\Delta E_{C1S} - E_0}{A}\right)^{\frac{1}{2}} C_l \quad (1)$$

In Eq. (1), OC is oxide concentration; ΔE_{C1S} is the binding energy (BE) shift between the C sp^2 peak and functional group C–OH (hydroxyl) peak; E_0 is the fundamental state of energy or energies imposed by the presence of carbon atoms; A is a parameter obtained from the fit and related to the energy value of $52.3eV$, it can be associated to a slope[56]; and C_l is independent of the energies and depends on a concentration due to the influence of the nuclei with a value of 0.122[56].

Figure 1b shows OC as a function of T_{CA}; as the synthesis temperature decreases, the OC increases from 0.21 (T_{CA} = 1273 K) to 0.28 (T_{CA} = 773 K). The fit corresponds to a linear relationship given by Eq. (2) and this behavior of OC (T_{CA}) can be attributed to oxides and organic compounds desorption. The negative slope probably indicates that the higher the synthesis temperature is, the more it promotes oxide and organic compounds desorption and, therefore, an OC decrease, as given by:

$$OC = -1.26 \times 10^{-4} * T_{CA} + 0.37. \quad (2)$$

Here, the values of $-1.26 \pm 0.01 \times 10^{-4} K^{-1}$ and 0.37 ± 0.01were related to the slope of Fig. 1b and the extrapolated value of OC at ideal $T_{CA} = 0K$; respectively, these parameters were obtained from the fitting of the experimental data, as presented in Fig. 1b by employing Eq. (2).

3.2. Compositional and morphological analyses

Figure 2a presents the normalized XPS spectra of 11 GOF samples synthesized to T_{CA} from 773 to 1273 K; peaks are observed at $\approx 538, 284eV$ associated with O1s and C1s respectively, evidencing the presence of carbon and oxygen atoms. Given that the general XPS spectra show the majority presence of carbon, as expected, high-resolution C1s and O1s spectra were performed for each of the 11 GOF samples. Figures 2b and 2c show the spectra corresponding to samples S-1173, with their respective deconvolution; the spectra were fitted by the Voigt function (GLP30). The C1s spectra show three bands in the BE range from 270 to 300 eV, these bands were associated with C sp^2 ($284.eV$) and C sp^3 ($285.2eV$) hybridization and functional group of C–OH ($286.4eV$)[39].

The O1s spectra generally show the presence of four bands in the range from 520 to 540 eV; these bands were associated with functional groups of C O ($531.9 \pm 0.1eV$), C–OH ($532.9 \pm 0.2eV$), C–O–C ($533.1 \pm 0.4eV$), and C–O ($534.2 \pm 0.1eV$), which supports the same interpretation and values reported by L. Stobinski *et al.*, in[39].

Figure 3 presents the SEM micrograph of GOF samples S-973; it is possible to observe fibers with porous tubular and rough surface, lengths in the order of $3mm$ and diameters of $600\mu m$, surface corrugations with a size of $40\mu m$, approximately, as presented in Fig. 3a. The cross-section of the microchannels was

observed with sizes varying from $1$to $20\mu m$, as shown in Fig. 3b, and Fig. 3c shows the surface roughness. The microchannels exhibited porous structures with sizes from 5 to $30\mu m$, as presented in Fig. 3d. This characteristic morphology was observed in all GOF samples studied herein and is typical behavior of GO obtained from RH, as described by Ahiduzzaman M. *et al.*, in[57].

3.3. Vibrational properties

The Raman spectra of the GOF samples obtained by varying the T_{CA} from 773 to 1273 K are shown in Fig. 4. Fitting and deconvolution of the Raman spectra served to identify the main vibrational contributions. The D-band ranged from 1329 to $1350cm^{-1}$ for samples with lowest OC (S-1273) and highest OC (S-773), respectively. The G-band varied from 1600 to $1589cm^{-1}$, for lowest OC and highest OC, respectively, as reported by T. Liou and P. Wang in[10]. The state of the D-band is caused by the presence of defects (disorders, vacancies, and functional groups) and, according to M.S. Ismail *et al.*, in[33], its height depends on the number of the sp^3 carbon atoms of graphene surface and the number of the defects of the graphene[42], while the G-band is caused by the formation of the stretching vibration sp^2 carbon atoms and represents the graphitized carbon[42]. These bands are characteristic of the Raman spectrum of GO, corresponding to the symmetry A1g and the vibrational mode of E2g, respectively[58], and overtone bands at high Raman shift of $2622cm^{-1}$ (2D band), $2875cm^{-1}$ (D + G band), and $3100cm^{-1}$ (2D' band), according to data reported in[25]. Broadening of these bands is related with the stacking effect of GO monolayers with edges, defects, and sp^2 regions[25].

3.4. Electrical properties

Figure 5a shows the electrical conductivity variation of GOF samples as a function of the OC. It was found that it decreases OC from 0.25 to 0.21 and increases electrical conductivity from 4.66×10^{-2} to $4.45Sm^{-1}$, as expected; this behavior, $\sigma = f(OC)$, is similar to that reported for graphene oxide obtained through other synthesis methods[41,45,53,59]. This increase can be attributed to the desorption of oxides and organic compounds via thermal decomposition, as a consequence of T_{CA}, which modifies the OC, as reported[60] and in graphene oxide nanofibers[59]. The experimental data of GOF electrical conductivity was fitted employing a polynomial function, as presented by the blue curve in Fig. 5a, as expected and to describe the $\sigma = f(OC)$ relation in a semiconductor material, as reported by Van Vechten[61]. Consequently, it was found that electrical conductivity as a function of OC in GOF samples is given by Eq. (3).

$$\sigma(x) = d + fx + gx^2. \quad (3)$$

Here, x is the independent variable associated with OC; d corresponds to electrical conductivity independent of the OC, with a value of $161.9 \pm 0.1S/m$; f was related with the linear factor of the OC that corresponds to a value of $-1268.4 \pm 0.1S/m$; and g is associated with the nonlinear factor of the

OC with a value of $2483.5 \pm 0.1 S/m$. The best fit was obtained with $R^2 = 0.97968$, as proposed here.

Equation (4) was used to calculate the E_g of the GOF samples, described by[23].

$$\sigma = \sigma_0 K_B T^* exp\left(\frac{E_g}{2K_B T}\right) \quad (4)$$

Where E_g is the band-gap energy, σ is the electrical conductivity of the GOF samples presented in Fig. 5a, σ_0 is the electronic conductivity independent of temperature, K_B is the Boltzmann constant, and T is the temperature.

As seen in Fig. 5b, the E_g of the GOF samples varies as a function of OC. Band-gap energy shows a variation from $0.24eV$ to $0.48eV$ by increasing the OC from 0.21 to 0.25, presenting similar behavior to that reported by theoretical studies, which have predicted that increased E_g is related with increased oxidation, as reported in[49,60,62–64]. The experimental data of $E_g\,(x)$ was fitted by employing a quadratic function. As illustrated by the red curve of Fig. 5b, it was found that the Van Vechten model describes the experimental results effectively, and it revealed that GOF samples exhibit semiconductor behavior, as expected and given by[61].

$$E_g\,(x) = a + bx + cx^2. \quad (5)$$

Here, $x$is the independent variable associated with OC; a corresponds to the E_g independent of the OC with a value of $8.1 \pm 0.1eV$; b was related with the linear factor of the OC that corresponds to a value of $-73.1 \pm 0.1eV$; and c is associated with the nonlinear factor of OC with a value of $170.8 \pm 0.1eV$. The best fit was obtained with $R^2 = 0.96052$. It is evident that OC modifies the electrical properties of GOFs, as expected[60,63,65–68].

In order to elucidate the possible mechanism responsible for semiconductor behavior in GOF samples, measured at room temperature, a correlation was conducted among the influence of OC with E_g and hydroxyl-epoxy ratio, as presented in Fig. 6. Previous studies reported that oxides in graphene are mainly hydroxyl and epoxy, as functional groups[63,65]; the presence of these oxides increase the interplanar distance[54,63,69]. The hydroxyl/epoxy ratio was estimated by employing the area comparison method of XPS spectra as $\left[1 - \left(\frac{A_{-O-}}{A_{OH}}\right)\right]$ for each GOF sample, as reported[70]. Figure 6 shows an $E_g\,(x)$ scale with hydroxyl/epoxy ratio, as a function of OC. Consequently, we believe that the presence of multifunctional oxides increases the E_g, as expected for a semiconductor material[64], and these changes in the electrical properties of GOF samples can be attributed to the formation at atomic scale of hydroxyl bridges promoted by experimental T_{CA}. The presence of hydroxyl bridges in GOF samples at an atomic

scale rearranges the graphene structure and out-of-plane carbon atoms, reducing the average interatomic distance opening the E_g, as reported on graphene oxide obtained from bamboo[70]. The experimental data of the hydroxyl/epoxy $\left(\frac{H}{E}\right)$ ratio was fitted by employing a polynomial function, as described by the green line in Fig. 6, given by the equation:

$$\left(\frac{H}{E}\right)(x) = m + nx + px^2.$$

(6)

Here, $x$is the independent variable associated with OC; m corresponds to the hydroxyl/epoxy ratio independent of the OC with a value of 12.9 ± 0.1; n was related with the linear factor of the OC that corresponds to a value of -121.9 ± 0.1; and p is associated with a nonlinear factor of the OC with a value of 289.5 ± 0.1. The best fit was obtained with $R^2 = 0.99641$, as proposed here.

The correlation between $\left(E_g\right)$ and hydroxyl/epoxy ratio, $\left(\frac{H}{E}\right)$, shows that decreased E_g from $0.48eV$ to $0.24eV$, increases $\frac{H}{E}$ from 0.11 to 0.58 (Fig. 6b). The experimental data of $\frac{H}{E}$ was fitted by using a linear function, as described by the red line in Fig. 6, given by the equation:

$$\left(\frac{H}{E}\right)(x) = q + rx.$$

(7)

Here, $x$is the independent variable associated with E_g; q corresponds to the $\frac{H}{E}$ independent of the E_g with a value of -0.36 ± 0.01; r was related with the linear factor of the $\frac{H}{E}$ that corresponds to a value of 1.92 ± 0.01. The best fit was obtained with $R^2 = 0.97257$, as proposed here.

3.5. Correlation among oxide concentrations, vibrational, and electrical properties

The Raman crystal size and boundary defect density were calculated by employing the equations (8) and (9), respectively, for each GOF sample at different T_{CA}, given by[23].

$$L_A\,(nm) = 4.4\left(\frac{I_G}{I_D}\right);$$

(8)

$$n_D{}^2\left(cm^{-2}\right) = 107.57 \times 10^{-9}\left(\frac{I_D}{I_G}\right).$$

(9)

Here, I_D is the normalized intensity of the D-band and I_G is the normalized intensity of the G-band. The increased $\frac{I_D}{I_G}$ ratio in equations (8) and (9) represents the transformation of a disordered structure into an ordered one, as expected. The correlation between OC and vibrational properties shows that a decreased OC increases the boundary defects density from 3.12 to $3.67 \times 10^{-4} cm^{-2}$, as presented in Fig. 7a, and decreases crystal size from 4.88 to $3.52 nm$, as shown in Fig. 7b. This can possibly be explained by the desorption of multifunctional oxides and some organic compounds due to thermal decomposition methods employed to synthesize GOF samples, as expected[71]. The experimental data the defects density was fitted by employing a linear function, as described by the blue line in Fig. 7a, given by the Eq. (10).

$$n_D \left(cm^{-2}\right)(x) = \alpha + \gamma x.$$

(10)

Where, $x$is the independent variable associated with OC; α corresponds to the independent term of the OC with a value of $5.62 \pm 0.01 cm^{-2}$; γ was related with the linear factor of the OC that corresponds to a value of $-9.13 \pm 0.01 cm^{-2}$. The best fit was obtained with $R^2 = 0.99361$, as proposed here. The experimental data the crystal size was fitted by employing a linear function, as described by the red line in Fig. 7b and given by:

$$L_A\,(nm)\,(x) = \delta + \epsilon x.$$

(11)

Here, $x$is the independent variable associated with OC; δ corresponds to the independent parameter of the OC with a value of $-1.33 \pm 0.1 nm$; ϵ was related with the linear factor of the OC that corresponds to a value of $22.47 \pm 0.1 nm$. The best fit was obtained with $R^2 = 0.99212$, as proposed here. The correlation between oxide concentration and vibrational properties can be described by expressions (10) and (11), as proposed here.

The correlation between electrical conductivity and vibrational properties, like defects density and crystal size, shows that increased electrical conductivity from 4.66×10^{-2} to $4.45 S/m$ increases defects density from 3.19×10^{-4} to $3.58 \times 10^{-4} cm^{-2}$ and decreases crystal size from 4.65 to $3.64 nm$, as presented in Figs. 7c and 7d. Thus, it can be deduced that low OC increases the characteristic relaxation time of the electric charge carrier dispersion process, while high OC decreases this characteristic time, due to a higher presence of impurities, mainly hydroxyl groups. These behaviors are very important, demonstrating that electrical and vibrational properties are tuned by OC; also, revealing the multifunctional effect of hydroxyl and epoxy groups present in GOF samples.

The experimental data the defects density was fitted by employing a polynomial function, as described by the red line in Fig. 7c and given by the Eq. (12).

$$n_D\left(cm^{-2}\right)(\sigma) = \xi + \phi\sigma + \nu\sigma^2.$$

(12)

Where, $\sigma$is the independent variable associated with electrical conductivity; ξ corresponds to the independent term of the electrical conductivity with a value of $3.35 \pm 0.01 cm^{-2}$; ϕ was related with the linear factor of the electrical conductivity, that corresponds to a value of $0.12 \pm 0.01 \frac{m}{S} cm^{-2}$; and ν is associated with the nonlinear factor of the electrical conductivity with a value of $-0.01 \pm 0.01 \frac{m^2}{S^2} cm^{-2}$. The best fit was obtained with $R^2 = 0.98047$, as proposed here.

The experimental data the crystal size was fitted by employing a polynomial function, as described by the blue line in Fig. 7d and given by:

$$L_A\,(nm)\,(\sigma) = \zeta + \rho\sigma + \epsilon\sigma^2.$$

(13)

Here, $\sigma$is the independent variable associated with electrical conductivity; ζ corresponds to the independent term of the electrical conductivity with a value of $4.21 \pm 0.01 nm$; ρ was related with the linear factor of the electrical conductivity that corresponds to a value of $-0.29 \pm 0.01 \frac{m}{S} nm$; and ϵ is associated with the nonlinear factor of the electrical conductivity with a value of $0.03 \pm 0.01 \frac{m^2}{S^2}\mathrm{nm}$. The best fit was obtained with $R^2 = 0.98079$, as proposed here. The correlation between electrical conductivity and vibrational properties can be described by expressions (12) and (13), as proposed here.

4. Conclusion

Graphene oxide fiber samples were synthesized from RH biomass, employing the first-stage thermal decomposition method. The experimental carbonization temperature varies the OC of GOF samples, and a linear relationship was found between these two synthesis parameters. The XPS spectra of GOF samples show two main peaks corresponding to C1s and O1s. It was found that decreased carbonization temperature increases oxygen content; the deconvolution of XPS spectra shows peaks for C1s corresponding to C sp^2, C sp^3, and C–OH, while for O1s, the main peaks are C–OH, C–O–C, and C–O. The GOF samples exhibit a morphology of fibers composed of porous structures with sizes between 5 and $30 \mu m$, the vibrational response of graphite oxide materials, with crystal size from 3.52 to $4.88 nm$ and the boundary defects density of $3.12–3.67 \times 10^{-4} cm^{-2}$. When OC decreases from 0.25 to 0.21, it increases electrical conductivity from 4.66×10^{-2} to $4.45 S/m$, decreases the E_g from $0.48 eV$ to $0.24 eV$, increases the defects density from 3.19×10^{-4} to $3.58 \times 10^{-4} cm^{-2}$, and decreases crystal size from 4.88 to $3.52 nm$; these behaviors are possibly attributed to the desorption of oxides and some organic compounds, as well as to the presence of hydroxyl and epoxy groups, by the oxidation processes. The correlation between E_g and hydroxyl/epoxy ratio suggests a semiconductor behavior of GOF samples, as expected and attributed to the presence of the hydroxyl bridges at atomic scale, which were

tuned by experimental T_{CA}. Likewise, the correlation between electrical conductivity and vibrational properties, such as defects density and crystal size, revealed that increased electrical conductivity increases defects density and decreases crystal size; this behavior may be attributed to increased characteristic relaxation time of the dispersive processes. This increases electrical conductivity by reducing OC, which reduces crystal size and, thus, increases boundary defects density in GOF samples. Consequently, the OC significantly affects the electronic structure and vibrational properties of GOF samples. By tuning OC, it was possible to control the electrical conductivity and the E_g. These results suggest that GOF samples are a possible candidate material for the development of advanced electronics of sensors and devices.

Declarations

Author contributions. JRC and JJP initiated the project. JRC carried out the synthesis and characterization of the materials. JRC and JJP discussed and the characterization results and the manuscript. JJP and JRC conducted calculation of band-gap energy in all samples. Furthermore, JRC and JJP wrote the manuscript with input from JJP.

Competing and financial interest. The authors declare no competing financial interests.

Data availability statement. The datasets used and/or analyzed during the current study available from the corresponding author on reasonable request.

Acknowledgments. The authors express sincere gratitude to Universidad de los Llanos, research project C01-F02-003-2017, the Interdisciplinary Institute of Sciences at Universidad del Quindío. This work was funded in part by Universidad del Quindío and MINCIENCIAS project SGR BPIN: 2020000100600 internal code 1112.

References

1. Melvin, G. J. H., Wang, Z., Siambun, N. J. & Rahman, M. M. Carbon materials derived from rice husks at low and high temperatures. IOP Conf. Ser. Mater. Sci. Eng. **217**, (2017).
2. Cao, G. *et al.* Carbon nanotubes with carbon blacks as cofillers to improve conductivity and stability. ACS Omega **4**, 4169–4175 (2019).
3. Tiwari, S. K., Sahoo, S., Wang, N. & Huczko, A. Graphene research and their outputs: Status and prospect. J. Sci. Adv. Mater. Devices **5**, 10–29 (2020).
4. Korkmaz, S. & Kariper, A. Graphene and graphene oxide based aerogels: Synthesis, characteristics and supercapacitor applications. J. Energy Storage **27**, (2020).
5. Prías-Barragán, J. J., Gross, K., Ariza-Calderón, H. & Prieto, P. Synthesis and vibrational response of graphite oxide platelets from bamboo for electronic applications. Phys. Status Solidi Appl. Mater. Sci. **213**, 85–90 (2016).

6. Teo, E. Y. L. *et al.* High surface area activated carbon from rice husk as a high performance supercapacitor electrode. Electrochim. Acta **192**, 110–119 (2016).
7. Azadeh, M., Zamani, C., Ataie, A. & Morante, J. R. Three-dimensional rice husk-originated mesoporous silicon and its electrical properties. Mater. Today Commun. **14**, 141–150 (2018).
8. Xu, Z. & Gao, C. Graphene fiber: A new trend in carbon fibers. Mater. Today **18**, 480–492 (2015).
9. Arifin, N. F. T. *et al.* Potential application of biomass derived graphene for COVID-19 pandemic. *Mater. Today Proc.* **46**, 1959–1962 (2020).
10. Liou, T. H. & Wang, P. Y. Utilization of rice husk wastes in synthesis of graphene oxide-based carbonaceous nanocomposites. Waste Manag. **108**, 51–61 (2020).
11. Xue, B. *et al.* The template effect of silica in rice husk for efficient synthesis of the activated carbon based electrode material. J. Alloys Compd. **789**, 777–784 (2019).
12. Raghavan, N., Thangavel, S. & Venugopal, G. A short review on preparation of graphene from waste and bioprecursors. Appl. Mater. Today **7**, 246–254 (2017).
13. Jin, H. *et al.* Synthesis of porous carbon nano-onions derived from rice husk for high-performance supercapacitors. Appl. Surf. Sci. **488**, 593–599 (2019).
14. Echeverry-Montoya, N. A. *et al.* Fabrication and electrical response of flexible supercapacitor based on activated carbon from bamboo. Phys. Status Solidi Curr. Top. Solid State Phys. **14**, (2017).
15. Khan, M. S. *et al.* Synthesis and evaluation of reduced graphene oxide for supercapacitor application. *Mater. Today Proc.* (2020) doi:10.1016/j.matpr.2020.05.403.
16. Bai, Y. *et al.* Preparation and application of cellulose gel in flexible supercapacitors. J. Energy Storage **42**, 103058 (2021).
17. Rhee, I., Lee, J. S., Kim, Y. A., Kim, J. H. & Kim, J. H. Electrically conductive cement mortar: Incorporating rice husk-derived high-surface-area graphene. Constr. Build. Mater. **125**, 632–642 (2016).
18. Chen, L. *et al.* Surface area measurements of graphene and graphene oxide samples: Dopamine adsorption as a complement or alternative to methylene blue? Appl. Mater. Today **18**, 100506 (2020).
19. Orsu, P. & Koyyada, A. Recent progresses and challenges in graphene based nano materials for advanced therapeutical applications: a comprehensive review. Mater. Today Commun. **22**, (2020).
20. Dhinakaran, V., Lavanya, M., Vigneswari, K., Ravichandran, M. & Vijayakumar, M. D. Review on exploration of graphene in diverse applications and its future horizon. *Mater. Today Proc.* **27**, 824–828 (2020).
21. Rybarczyk, M. K. *et al.* Hard carbon derived from rice husk as low cost negative electrodes in Na-ion batteries. J. Energy Chem. **29**, 17–22 (2019).
22. Yu, K. *et al.* Synthesis of zinc-cobalt bimetallic oxide anchored on the surface of rice husk carbon as anode for high-performance lithium ion battery. J. Phys. Chem. Solids **135**, 109112 (2019).
23. Prías-Barragán, J. J., Gross, K., Ariza-Calderón, H. & Prieto, P. Transport Mechanisms Study in Graphene Oxide Multi-Layers Obtained From Bamboo As Source Material and Pos-Sible. Rev. Divulg.

Científica y Tecnológica del Inst. Interdiscip. las Ciencias **1**, 9–47 (2018).

24. Wang, G., Wang, D., Kuang, S., Xing, W. & Zhuo, S. Hierarchical porous carbon derived from rice husk as a low-cost counter electrode of dye-sensitized solar cells. Renew. Energy **63**, 708–714 (2014).
25. Arias-Niquepa, R. A., Prías-Barragán, J. J., Ariza-Calderón, H. & Rodríguez-García, M. E. Activated Carbon Obtained from Bamboo: Synthesis, Morphological, Vibrational, and Electrical Properties and Possible Temperature Sensor. Phys. Status Solidi Appl. Mater. Sci. **216**, 1–11 (2019).
26. Zheng, Q., Lee, J., Shen, X., Chen, X. & Kim, J.-K. Graphene-based wearable piezoresistive physical sensors. Mater. Today **36**, 158–179 (2020).
27. Ikram, R., Jan, B. M. & Ahmad, W. Advances in synthesis of graphene derivatives using industrial wastes precursors; prospects and challenges. J. Mater. Res. Technol. **9**, 15924–15951 (2020).
28. Razaq, A. *et al.* Review on Graphene-, Graphene Oxide-, Reduced Graphene Oxide-Based Flexible Composites: From Fabrication to Applications. Materials (Basel). **15**, (2022).
29. Goswami, S., Banerjee, P., Datta, S., Mukhopadhayay, A. & Das, P. Graphene oxide nanoplatelets synthesized with carbonized agro-waste biomass as green precursor and its application for the treatment of dye rich wastewater. Process Saf. Environ. Prot. **106**, 163–172 (2017).
30. Castro-Ladino, J. R., Vacca-Casanova, A. B. & Cuy-Hoyos, C. A. Pyrolysis system to obtain carbonaceous material from rice husk used as a precursor. Rev. la Acad. Colomb. Ciencias Exactas, Fis. y Nat. **44**, 805–813 (2020).
31. Marcano, D. C. *et al.* Improved synthesis of graphene oxide. ACS Nano **4**, 4806–4814 (2010).
32. Chen, J., Yao, B., Li, C. & Shi, G. An improved Hummers method for eco-friendly synthesis of graphene oxide. Carbon N. Y. **64**, 225–229 (2013).
33. Ismail, M. S. *et al.* Synthesis and characterization of graphene derived from rice husks. Malaysian J. Fundam. Appl. Sci. **15**, 516–521 (2019).
34. Singh, P., Bahadur, J. & Pal, K. One-Step One Chemical Synthesis Process of Graphene from Rice Husk for Energy Storage Applications. Graphene **06**, 61–71 (2017).
35. Prías-Barragán, J. J., Echeverry-Montoya, N. A. & Ariza-Calderón, H. Fabricación y caracterización de carbón activado y de nanoplaquetas de carbón a partir de Guadua angustifolia Kunth para aplicaciones en electrónica. Rev. la Acad. Colomb. Ciencias Exactas, Físicas y Nat. **39**, 444 (2015).
36. Weldekidan, H., Strezov, V., Town, G. & Kan, T. Production and analysis of fuels and chemicals obtained from rice husk pyrolysis with concentrated solar radiation. Fuel **233**, 396–403 (2018).
37. Souza, C. B. de *et al.* Evolution of dielectric properties of thermally reduced graphene oxide as a function of pyrolisis temperature. Diam. Relat. Mater. **93**, 241–251 (2019).
38. Smith, A. T., LaChance, A. M., Zeng, S., Liu, B. & Sun, L. Synthesis, properties, and applications of graphene oxide/reduced graphene oxide and their nanocomposites. Nano Mater. Sci. **1**, 31–47 (2019).
39. Stobinski, L. *et al.* Graphene oxide and reduced graphene oxide studied by the XRD, TEM and electron spectroscopy methods. J. Electron Spectros. Relat. Phenomena **195**, 145–154 (2014).

40. Claoston, N., Samsuri, A. W., Ahmad Husni, M. H. & Mohd Amran, M. S. Effects of pyrolysis temperature on the physicochemical properties of empty fruit bunch and rice husk biochars. Waste Manag. Res. **32**, 331–339 (2014).
41. Wang, Y. *et al.* Reduced graphene oxide film with record-high conductivity and mobility. Mater. Today **21**, 186–192 (2018).
42. Li, W. *et al.* Hard carbon derived from rice husk as anode material for high performance potassium-ion batteries. Solid State Ionics **351**, 115319 (2020).
43. Liang, S., Yu, K., Li, Y. & Liang, C. Rice husk-derived carbon@SnO2@graphene anode with stable electrochemical performance used in lithium-ion batteries. Mater. Res. Express **7**, (2019).
44. Manuvinakurake, M., Gandhi, U., Mangalnathan, U. & Nayak, M. M. Reduced Graphene oxide strain gauge sensor for dynamic pressure sensing. 2018 *4th IEEE Int. Conf. Emerg. Electron. ICEE 2018* 2018–2021 (2018) doi:10.1109/ICEE44586.2018.8937906.
45. Liu, W. & Speranza, G. Tuning the Oxygen Content of Reduced Graphene Oxide and Effects on Its Properties. ACS Omega **6**, 6195–6205 (2021).
46. Díez-pascual, A. M., Sainz-urruela, C., Vallés, C., Vera-lópez, S. & Andrés, M. P. S. Tailorable synthesis of highly oxidized graphene oxides via an environmentally-friendly electrochemical process. Nanomaterials **10**, 1–18 (2020).
47. Morimoto, N., Kubo, T. & Nishina, Y. Tailoring the oxygen content of graphite and reduced graphene oxide for specific applications. Sci. Rep. **6**, 4–11 (2016).
48. Krishnamoorthy, K., Veerapandian, M., Yun, K. & Kim, S. J. The chemical and structural analysis of graphene oxide with different degrees of oxidation. Carbon N. Y. **53**, 38–49 (2013).
49. Boukhvalov, D. W. & Katsnelson, M. I. Modeling of graphite oxide. J. Am. Chem. Soc. **130**, 10697–10701 (2008).
50. Minitha, C. R., Nivedita, L. R., Asokan, K. & Rajendra Kumar, R. T. Tuning the electrical properties of graphene oxide by nitrogen ion implantation: Implication for gas sensing. Nucl. Instruments Methods Phys. Res. Sect. B Beam Interact. with Mater. Atoms **450**, 257–261 (2019).
51. Ashery, A., Moussa, M. A. & Turky, G. M. Synthesis, characterization and electrical properties of conducting nanoparticles of graphene oxide. *Mater. Today Proc.* **44**, 3017–3024 (2021).
52. Silipigni, L. *et al.* Temperature and environment effects on the graphene oxide reduction via electrical conductivity studies. J. Mater. Sci. Mater. Electron. **31**, 11847–11854 (2020).
53. Venugopal, G., Krishnamoorthy, K. & Kim, S. J. An investigation on high-temperature electrical transport properties of graphene-oxide nano-thinfilms. Appl. Surf. Sci. **280**, 903–908 (2013).
54. Wang, H. & Hu, Y. H. Effect of oxygen content on structures of graphite oxides. Ind. Eng. Chem. Res. **50**, 6132–6137 (2011).
55. Al-Gaashani, R., Najjar, A., Zakaria, Y., Mansour, S. & Atieh, M. A. XPS and structural studies of high quality graphene oxide and reduced graphene oxide prepared by different chemical oxidation methods. Ceram. Int. **45**, 14439–14448 (2019).

56. Carvalho, A. *et al.* The degree of oxidation of graphene oxide. Nanomaterials **11**, 1–8 (2021).
57. Ahiduzzaman, M. & Sadrul Islam, A. K. M. Preparation of porous bio-char and activated carbon from rice husk by leaching ash and chemical activation. Springerplus **5**, (2016).
58. Johra, F. T., Lee, J. W. & Jung, W. G. Facile and safe graphene preparation on solution based platform. J. Ind. Eng. Chem. **20**, 2883–2887 (2014).
59. Huang, H. D., Guo, Z., Yang, P. yan, Chen, P. & Wu, J. Electrical conductivity and hydrophobicity of graphene oxide-modified carbon nanofibers. Chem. Phys. Lett. **771**, 138551 (2021).
60. Gross, K. *et al.* Electrical conductivity of oxidized-graphenic nanoplatelets obtained from bamboo: Effect of the oxygen content. Nanotechnology **27**, (2016).
61. Van Vechten, J. A. & Bergstresser, T. K. Electronic structures of semiconductor alloys. Phys. Rev. B **1**, 3351–3358 (1970).
62. Acik, M. & Chabal, Y. J. A Review on Reducing Graphene Oxide for Band Gap Engineering. J. Mater. Sci. Res. **2**, (2012).
63. Huang, H., Li, Z., She, J. & Wang, W. Oxygen density dependent band gap of reduced graphene oxide. J. Appl. Phys. **111**, (2012).
64. Prías Barragán, J. J. *et al.* Graphene Oxide Thin Films: Synthesis and Optical Characterization. ChemistrySelect **5**, 11737–11744 (2020).
65. Jia, T. T., Sun, B. Z., Lin, H. X., Li, Y. & Chen, W. K. Bonding of hydroxyl and epoxy groups on graphene: Insights from density functional calculations. Jiegou Huaxue **32**, 1475–1484 (2013).
66. Yan, J. A. & Chou, M. Y. Oxidation functional groups on graphene: Structural and electronic properties. Phys. Rev. B - Condens. Matter Mater. Phys. **82**, 21–24 (2010).
67. Sharma, N. *et al.* Investigation of bandgap alteration in graphene oxide with different reduction routes. Appl. Surf. Sci. **513**, 145396 (2020).
68. Prias-Barragan, J. J., Gross, K., Ariza-Calderon, H. & Prieto, P. Graphene oxide multilayers: Synthesis, properties and possible applications in electronics. Lat. Am. Electron Devices Conf. LAEDC *2019* (2019) doi:10.1109/LAED.2019.8714743.
69. Lahaye, R. J. W. E., Jeong, H. K., Park, C. Y. & Lee, Y. H. Density functional theory study of graphite oxide for different oxidation levels. Phys. Rev. B - Condens. Matter Mater. Phys. **79**, 1–8 (2009).
70. Prías-Barragán, J. J. *et al.* Magnetism in graphene oxide nanoplatelets: The role of hydroxyl and epoxy bridges. J. Magn. Magn. Mater. **541**, (2022).
71. Prías-Barragán, J. J. *et al.* Room-temperature ferromagnetism in oxidized-graphenic nanoplatelets induced by topographic defects. J. Magn. Magn. Mater. **524**, (2021).

Figures

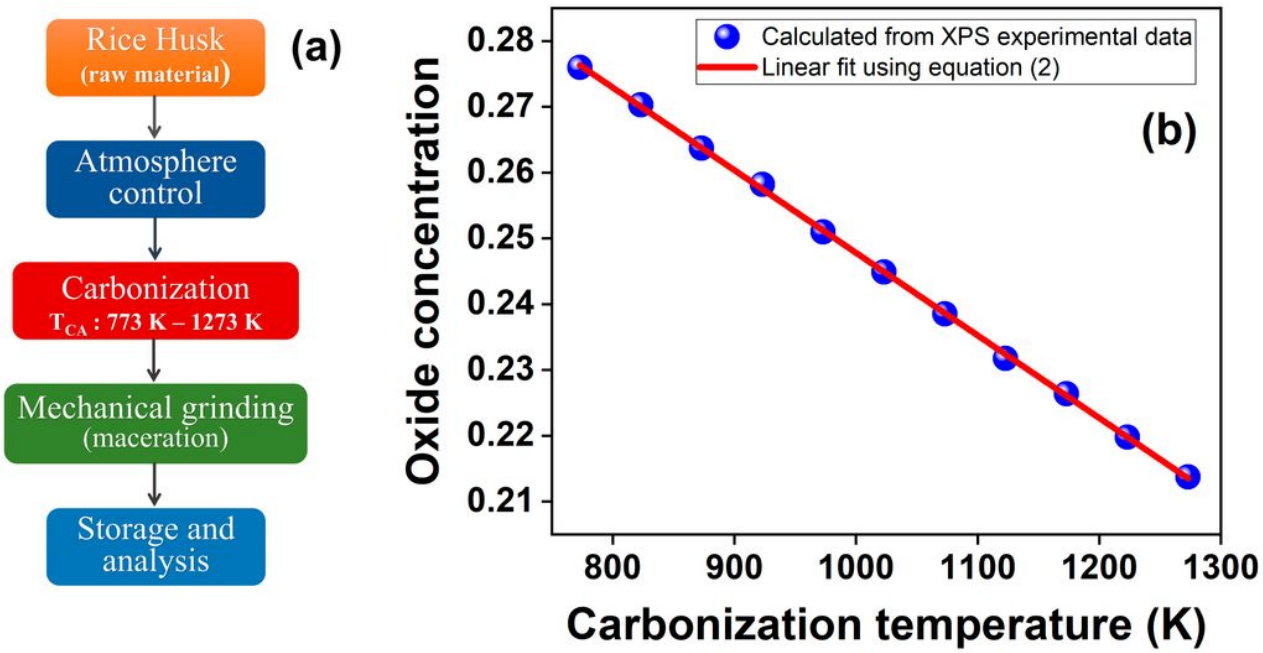

Figure 1

(a) Schematics of the process to prepare GOF samples. (b) Carbonization temperature influence in OC of GOF samples obtained by varying T_{CA} from 773 to 1273 K.

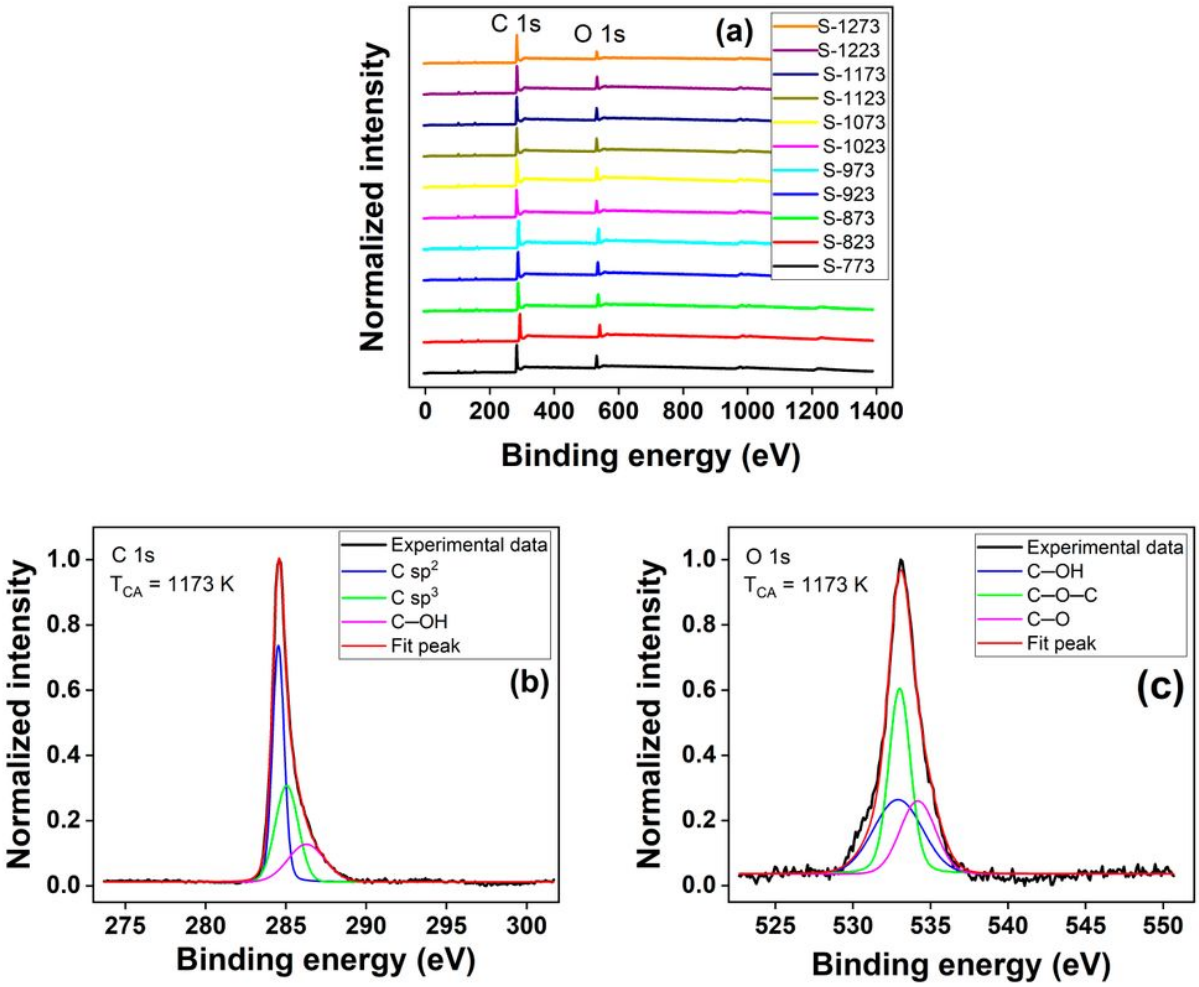

Figure 2

XPS spectra of: (a) GOF samples synthesized to T_{CA} from 773 to 1173 K. (b). High-resolution C1s spectra, and (b). High-resolution O1s spectra of S-1173.

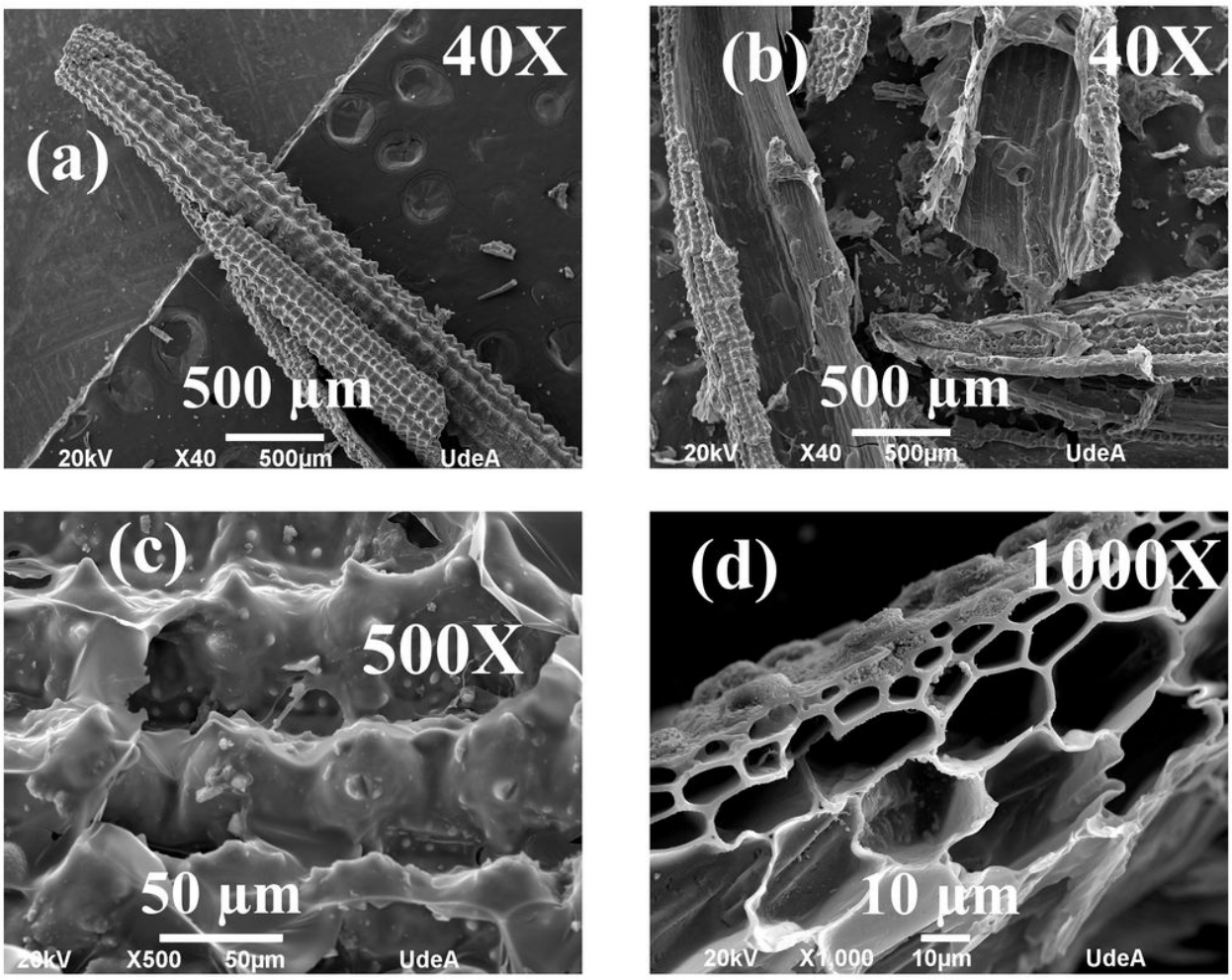

Figure 3

SEM micrographs of GOF samples S-973, the scale at (a) 500 *µm* 40X, (b) 500 *µm* 40X, (c) 50 *µm* 500X, (d) 10 *µm* 1000X.

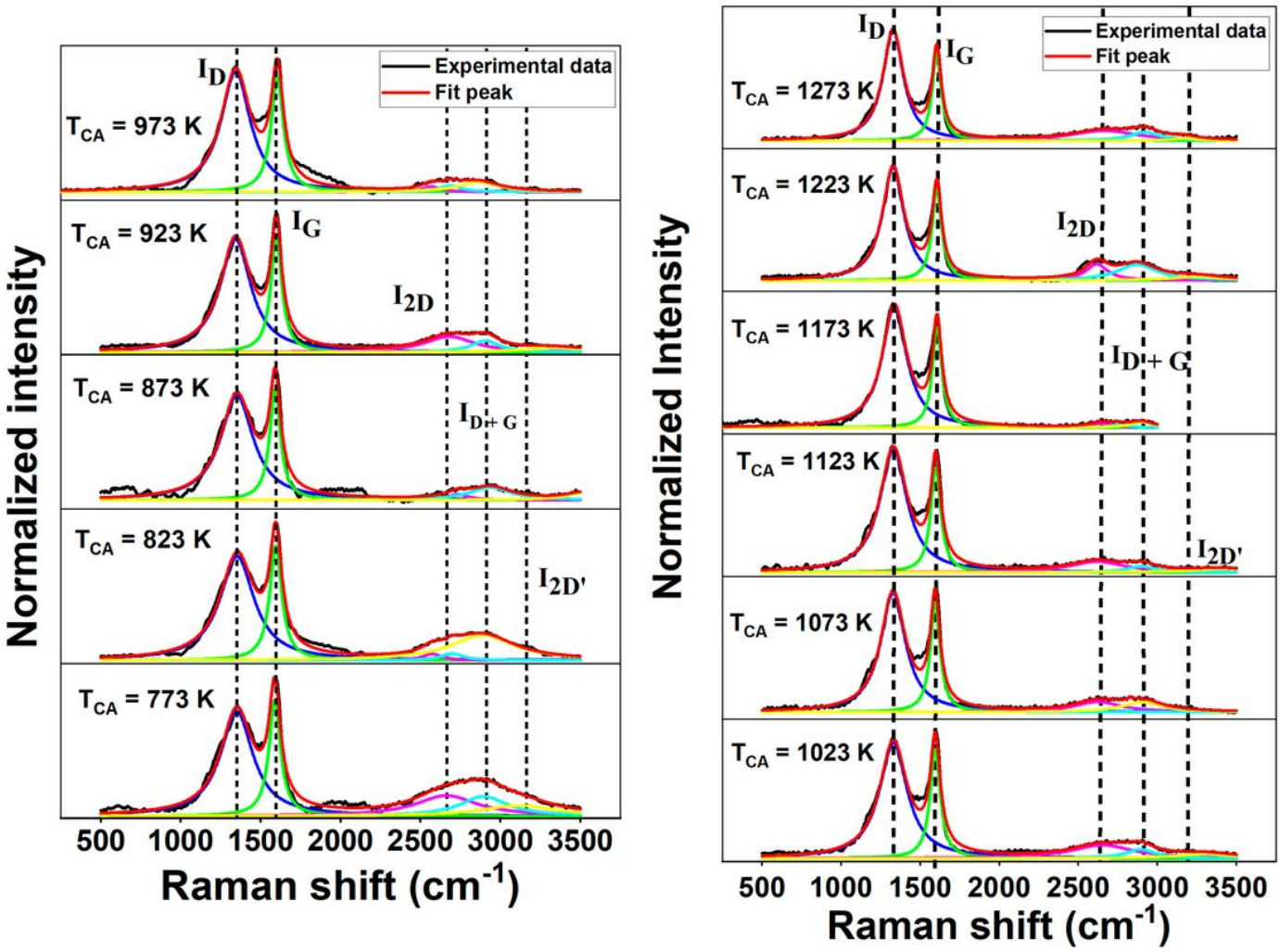

Figure 4

Raman spectra of GOF samples obtained by varying T_{CA} from 773 to 1273 K.

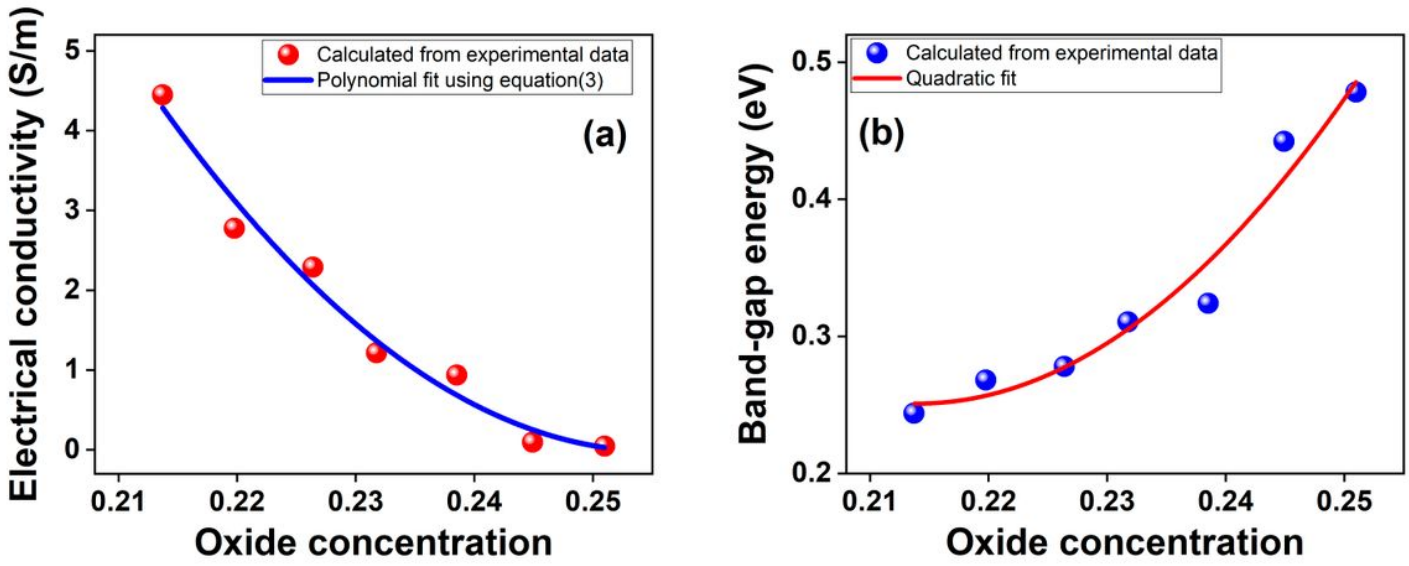

Figure 5

Influence of OC on: (a) Electrical Conductivity and (b) Band-gap Energy of GOF samples.

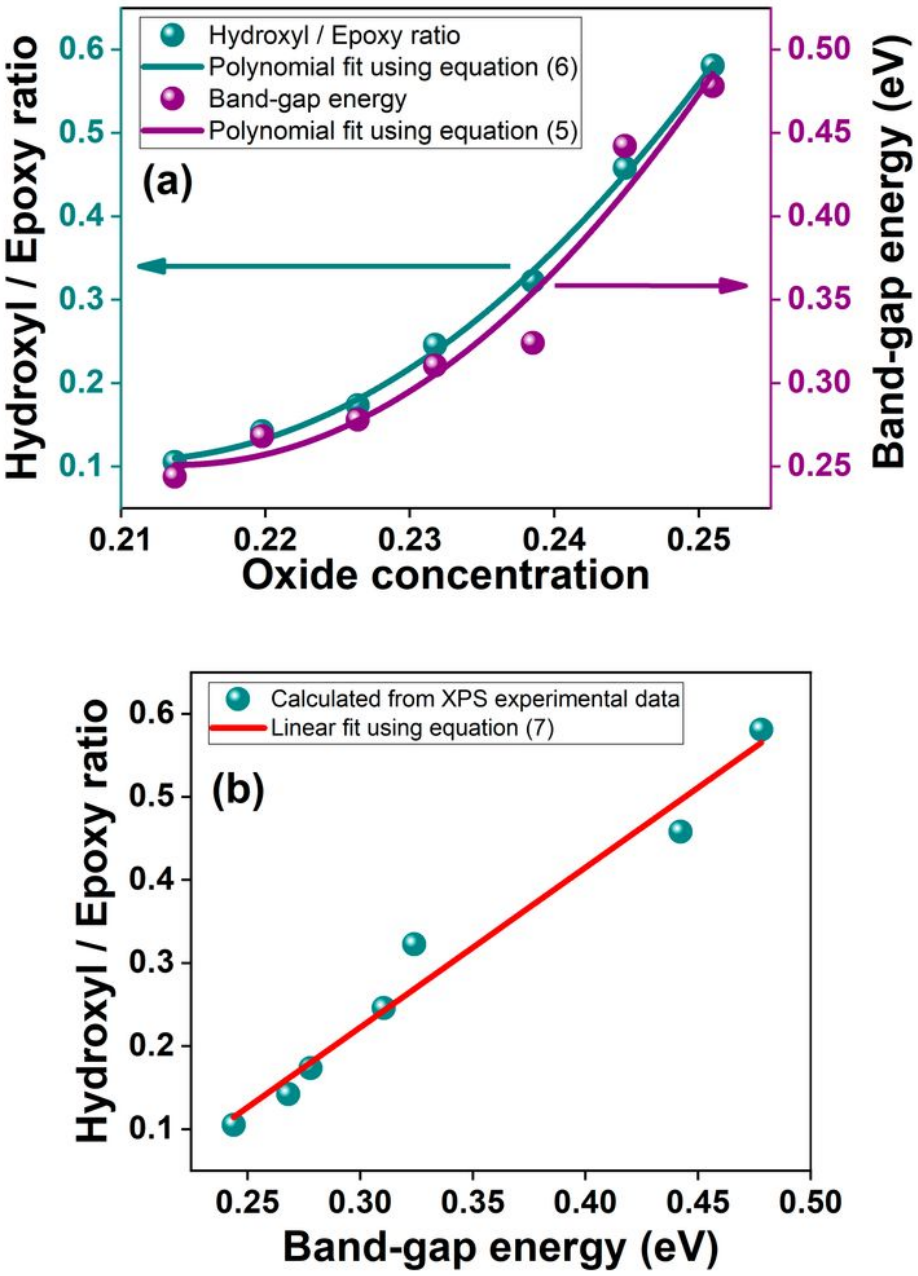

Figure 6

(a) Influence of OC on Eg and hydroxyl/epoxy ratio, (b) Correlation between Eg and hydroxyl/epoxy ratio in GOF samples.

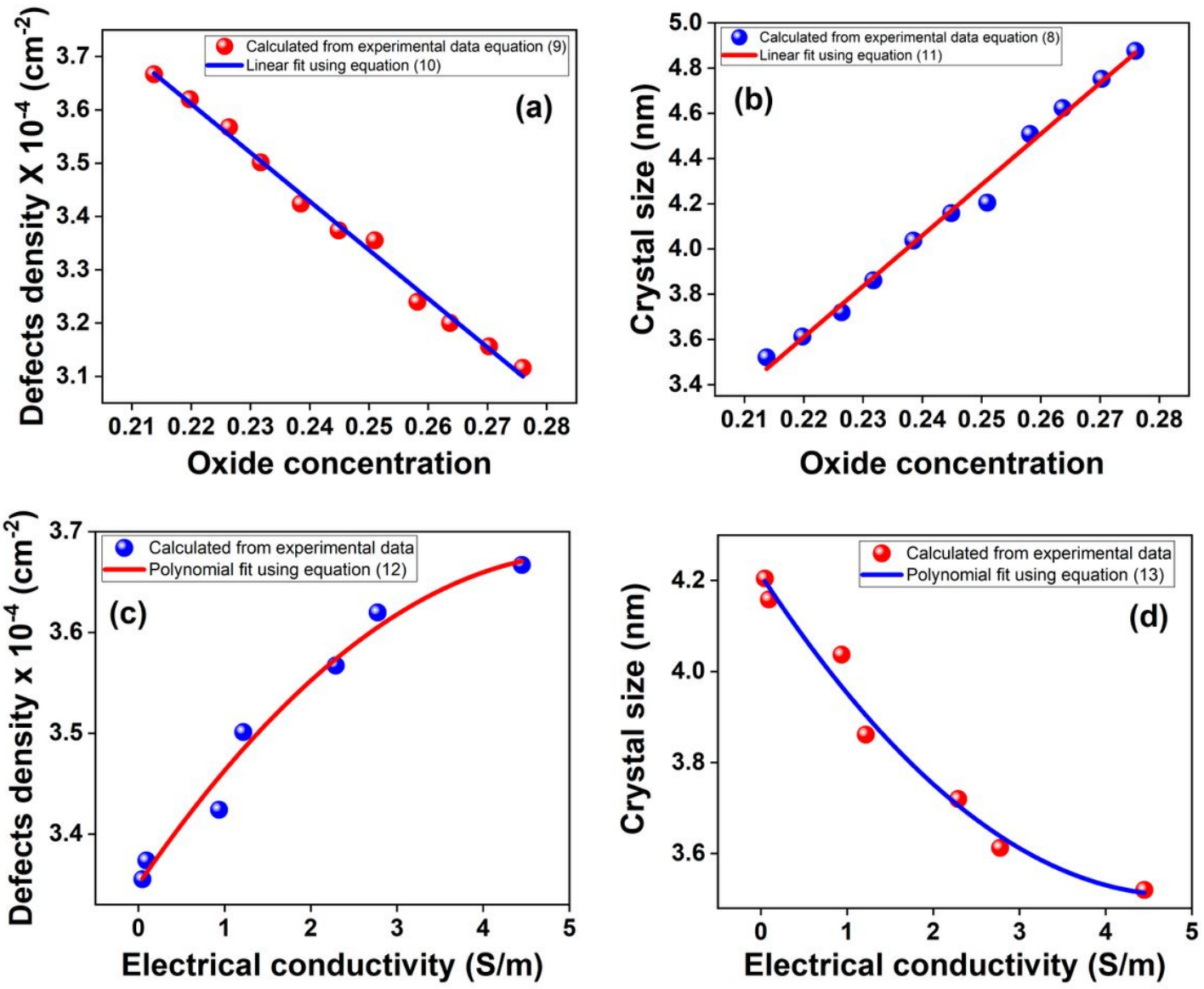

Figure 7

Correlation among OC and (a) Defects density and (b) Crystal size; and correlation among electrical conductivity and (c) Defects density and (d) Crystal size of GOF samples.